



On the determination of diffusion coefficients in two-component alloys and doped semiconductors. Several implications concerning the International Space Station



O. Sánchez^a, X. Ruiz^{b,c}, M. Pujalte^b, I. Mercader^{a,*}, O. Batiste^a, Jna. Gavaldà^b

^a *Departament de Física Aplicada, Universitat Politècnica de Catalunya, UPC, Barcelona, Spain*

^b *Departament de Química Física i Inorgànica, Universitat Rovira i Virgili, URV, Tarragona, Spain*

^c *Institut d'Estudis Espacials de Catalunya, IEEC, Barcelona, Spain*

ARTICLE INFO

Article history:

Received 10 July 2014

Received in revised form 22 January 2015

Accepted 23 February 2015

Keywords:

Diffusion coefficients
Numerical simulation
Microgravity conditions
Melted semiconductors
Liquid metals
Shear cell
Long capillaries

ABSTRACT

The accurate determination of mass diffusion coefficients is a technologically relevant problem that has implications on the modelling and control of material processes such as crystal growth and casting. It is also important in the validation of different theories of atomic diffusion. The experimental determination of these coefficients, when there is a liquid phase, is difficult due to the unavoidable presence of buoyancy driven convection currents that enhance mass transport and disturb diffusion measurements. To minimize as much as possible these problems, long capillaries are used in order to confine the fluid and reduce the intensity of the convective motions. These measurements have also been done in reduced gravity environments, but the residual gravity may still be able to induce buoyancy driven convection motions. The aim of our work is to analyze the impact of low solutal Rayleigh number environments on the accuracy of the interdiffusion coefficient measurements using long capillaries. In the present study we deal with two liquid systems; photovoltaic silicon and Al-based liquid binary alloys at high temperature. We have numerically simulated two different experimental techniques used to determine the diffusion coefficients; the shear cell and the long capillary techniques. We also consider the effect of rotating the cylindrical cell along their axis as a mechanism to reduce axial convective transport even in Earth laboratories. Finally, we use typical accelerometric signals from the International Space Station (ISS) in the quasi-steady range of frequencies. The signals concentrate on typical station reboots because the accelerometric level of the rest of potentially dangerous disturbances – dockings, undockings and Extra Vehicular Activities, EVAs – is considerably lower.

© 2015 Elsevier Ltd. All rights reserved.

1. Introduction

The accurate determination of mass diffusion coefficients in high temperature doped melts and two-component liquid mixtures, is of fundamental importance in the simulation and optimal control of solidification processes. Diffusion coefficients are usually treated as constants in computational growth models, but real systems with large segregation coefficients exhibit concentration and position dependent diffusion coefficients due to the strong gradients that exist at the growing interfaces. In addition, concentration gradients are correlated with chemical potential gradients, so it is very important to determine experimentally these relationships in order to apply them to predictive growth models. The experimental determination of diffusion coefficients is also important from a

theoretical perspective for the validation of different theories that predict how these coefficients depend on temperature and concentration.

Diffusion coefficients at high temperature are usually measured on Earth laboratories typically using diffusion couple arrangements inside long capillaries [1]. An initial concentration profile in the form of a step (diffusion couple) is left to diffuse during a certain time, then the final concentration profile is compared to the analytical solution obtained using Fick's law and the required diffusion coefficient compatible with this profile is calculated [2,3]. There are two main experimental techniques used to prepare and analyze diffusion experiments, the shear cell method (hereafter SC) and long capillary technique (hereafter LC). In the SC method, the diffusion experiment begins by joining two capillary segments with different composition. At the end of the experiment the cell is divided in slices that are individually moved

* Corresponding author.

Nomenclature

A	amplitude	Sc	Schmidt number ($Sc = \nu/D$)
C^*	concentration of the denser component	t	nondimensional time
C_0^*	mean value of the concentration	t_{end}	nondimensional end time
C	rescaled concentration of the denser component	\vec{V}	velocity field
C_i	averaged concentration in segment i	x, y, z	cartesian coordinates
ΔC^*	difference between maximum and minimum concentration at $t = 0$ [mol m^{-3}]	r, θ, z	cylindrical components
D	diffusion coefficient [$\text{m}^2 \text{s}^{-1}$]	z_i	axial position of the center of the shear cell segment i
$D^*(t)$	apparent diffusion coefficient [$\text{m}^2 \text{s}^{-1}$]	Greek letters	
$\%D^*(t)$	standard non-dimensional indicator	α	angle between the gravity vector and the gradient of concentration
$\%D^*(t_{end})$	uncorrected final indicator at the end time	β_c	solubility expansion coefficient [$\text{m}^3 \text{mol}^{-1}$]
$\%D_{diff}^*(t_{end})$	zero error due to the methodology used (diffusive case at the end time)	Γ	aspect ratio
$\%D(t_{end})$	corrected non-dimensional indicator at the end time	λ	length scale [m]
$\langle E_k \rangle$	mean kinetic energy	ν	kinematic viscosity [$\text{m}^2 \text{s}^{-1}$]
f	nondimensional external frequency	Ω	nondimensional axial rotation rate
g	gravity level [m s^{-2}]	τ	time scale [s]
L	capillary cell length [m]	τ_i	thruster ignition time [s]
p	pressure		
R_c	radius of the cylinder [m]		
Ra	solubility Rayleigh number $\left(Ra = \frac{\beta_c \Delta C^* \lambda^3}{\nu D} \right)$		

perpendicularly to their axis. In this way, when the diffusion process is stopped, the slices are separated and cooled until they solidify, and the concentration of each solidified slice enables to accurately reconstruct the final concentration profile needed (*post mortem* analysis) [4]. In the long capillary technique (LC), a diffusion couple previously prepared is placed in the long cylindrical cell and introduced in a furnace until the solute has diffused for a certain time, then the specimen is quenched and analyzed using Atomic Absorption Spectrophotometry (AAS). A recently developed direct procedure using X-ray radioscopic techniques, allows *in-situ* instantaneous measurements of the concentration profiles by taking absorption pictures of the experiments [5–7]. There exist other less popular possibilities such as the so-called Axial Heat Processing (AHP), a crystal growth methodology which tries to control thermal conditions near the growing interface to minimize natural convection. The segregation in the solid grown phase is then used as a basis for the subsequent diffusion analyses [8–12].

In the last years, mass diffusion experiments have been made in low gravity environments [13–17] to avoid the disturbing effect of buoyancy generated convection, but the residual gravity and g-jitter are still able to induce fluid motions that distort the measurements [18–21]. To assess the real importance of such effects, the acceleration environment must be characterized in detail and numerical models will then be used to carefully evaluate the flow impact on diffusion measurements. In the present work we will study the effect of low levels of gravity on diffusion experiments, we will consider the effect of cell inclination, oscillating gravity, the rotation of the cell and of real accelerometric signals. Our methodology will consist in performing numerical simulations of

the capillary cells and compare the final states with the expected ones by a pure diffusive process without convection. As it has been mentioned before, in shear cell simulations the comparisons will use the averaged concentration of each segment of the cell while in the simulation of the long capillary technique we will use the continuous concentration profiles all along the capillary. The present numerical experiments can deal with both types of concentration measurements without problems. In previous works the system has been modeled as a long rectangular domain [2,3], here we will consider a more realistic 3D cylindrical domain and compare the results with the 2D case.

Due to their unquestionable technological interest we focus the study on two different kinds of materials, photovoltaic silicon (PV-Si) and aluminum based alloys. Concerning multi-crystalline ingots of photovoltaic silicon, PV-Si, the knowledge of the diffusion coefficients of dopants and impurities is of capital importance to improve the predictions of the present computational models of directional solidification [22–31]. For economic reasons, Upgraded Metallurgical Grade Silicon, UMG-Si, is progressively replacing the more expensive ultra pure Electronic Grade Silicon, EG-Si, as feedstock material in ingot casting processes, but UMG-Si contains a high amount of the above-mentioned dopants, metallic and non-metallic impurities, which strongly interact with crystal defects in the resulting multi-crystalline ingots (see Table 1). Concerning metallic alloys, in particular, Al-based alloys, diffusion and its relation to thermodynamics plays a capital role in nucleation theories and in the correct predictions of the coupled macro-meso-microscopic computational models of solidification [32,33].

Table 1
Effect of dopants, metallic and non-metallic impurities in the processing of PV-Si.

Metallic impurities (Al, Bi, Ga, In, ...)	UMG-Si feedstock	Point defects (scarcely incorporated during solidification because of the very low values of their segregation coefficients)	Decreasing of efficiency due to minority carriers (electrons) recombination
Non-metallic impurities	O UMG-Si feedstock (SiO_2 particles) (dissolution of SiO_2 -crucible in mono-crystalline Czochralski growth)	Oxide and silicide particles could act as getter centers for metallic impurities	Degradation of the solar cell during illumination
	C Graphite heaters (CO in the near atmosphere)	Formation of SiC clusters (evaporation of SiO_2 at the melt surface)	Decrease of the electric properties
	N Si_3N_4 coating of fused silica crucibles (dissolution of the Si_3N_4 layer)	Si_3N_4 formation (acting as nuclei for SiC clusters)	SiC clusters can act as electrical shunts (also, wire breakings during the wire sawing process)

The paper is organized as follows: in Section 2, we will describe the governing equations and the numerical methods used; in Section 3, the results corresponding to typically low solutal Rayleigh number environments (Section 3.1) as well as the ones corresponding to real accelerometric records coming from the International Space Station (Section 3.2) will be presented. Finally, the conclusions of the study will be summarized in Section 4.

2. Governing equations and numerical procedures

To model the problem we use a closed cylinder, filled with a two-component liquid mixture. Due to the fact that the furnaces used in real experiments at high temperature have a very low thermal gradient [14], [34] we consider the system to be isothermal and focus on the solution of the solutal problem. Under the conditions of the present work, the shear effects are negligible when considering the shear cell technique [35–37], and will not be taken into account.

We consider the so-called interdiffusion couple configuration [3]. In this case the diffusion is driven by the existence of two half parts with different initially uniform concentrations, located symmetrically at both sides of the cell (see Fig. 1). This system is analyzed using the transport equation for mass coupled to the incompressible Navier–Stokes equations in the Boussinesq approximation. In this way we are able to consider the effect of the convection currents induced by the density variations caused by concentration differences. The equations written in nondimensional form are

$$\nabla \cdot \vec{V} = 0 \tag{1.a}$$

$$\frac{\partial \vec{V}}{\partial t} + (\vec{V} \cdot \nabla) \vec{V} = -\nabla p + Sc \nabla^2 \vec{V} + Ra \cdot Sc \cdot C \tag{1.b}$$

$$\frac{\partial C}{\partial t} + \vec{V} \cdot \nabla C = \nabla^2 C. \tag{1.c}$$

Here \vec{V} is the non-dimensional velocity and C is the non-dimensional rescaled concentration defined as $C = (C^* - C_0^*)/\Delta C^*$, where C^* is the concentration of the denser component, ΔC^* is the initial concentration difference and C_0^* is its mean value. The length scale λ used to obtain the previous non-dimensional variables is the diameter $\lambda = 2R$ of the cylindrical cell. The time scale τ is the dimensional group λ^2/D , being D the mass diffusion coefficient. The other parameters appearing in the equations are the vector solutal Rayleigh number \vec{Ra} , and the Schmidt number Sc , respectively defined as

$$\vec{Ra} = \frac{\vec{g} \beta_c \Delta C^* \lambda^3}{\nu D}, \quad Sc = \frac{\nu}{D},$$

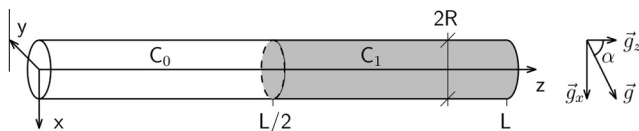


Fig. 1. Sketch of the long cylindrical capillary with the initial diffusion couple in place.

where β_c is the solutal expansion coefficient, ν is the kinematic viscosity and \vec{g} is the gravity vector. In the cylindrical cell the coordinate system of the problem has been chosen in such a way that the positive z axis coincides with the axis of the cylinder directed from lower to higher concentration, the gravity is contained in the plane $y = 0$ (except in Section 3.2), and the origin of coordinates is on the center of the base of the cylinder with lower concentration (see Fig. 1). The cylindrical cell is characterized by its aspect ratio, $\Gamma = L/2R$ (L is the length of the cell), that is chosen as $\Gamma = 40$ in the present calculations. The velocity field obeys a no-slip boundary condition at the walls, which have been considered impermeable to solute transport.

Table 2 defines the typical quantitative values for the two materials considered, photovoltaic silicon and aluminum-based alloys, taking into account real values extracted from the specialized literature, references [38–42] for PV-Si and references [43–46] for aluminum-based alloys. All these values have been considered constant, i.e. independent on the composition. To accomplish this last hypothesis, the initial quantitative difference between the concentrations of both sides of the cell has been limited to a reasonable threshold value of the order of 5 wt%. Also Table 2 shows the geometrical values needed to dimensionally define the computational domain, the length, L and the diameter $2R$ respectively.

We have solved the transport equations using two different numerical methods; a finite volume and a pseudospectral method, in order to model the two different experimental techniques, SC (shear cell technique) and LC (long capillary technique) respectively. The finite volume method uses a second-order central scheme for the spatial discretization of the diffusive and convective terms and it performs the time integration using a Crank–Nicolson scheme. The coupling between the velocity and pressure fields is solved with a fractional step method and the resulting Poisson equation is solved using the biconjugate gradient method [2,3,47,48]. The pseudospectral method uses the algorithm described in [49], which can be summarized as follows. To integrate the equations in time, we use the second order time-splitting method proposed in [50], where the pressure boundary condition and a stiffly stable scheme prevent the propagation and accumulation of time difference errors [51]. For the spectral spatial discretization, we use a Galerkin–Fourier method in the azimuthal direction and Chebyshev collocation in radial and axial directions (Gauss–Lobatto points). The radial dependence of the functions is approximated by a Chebyshev expansion between $-R$ and R , but forcing the proper azimuthal parity of the variables at the origin [52,53]. For instance, the concentration field and the axial component of the velocity has an even parity, whereas the radial and azimuthal components of the velocity field are odd functions. To avoid including the origin in the mesh grid, we use an odd number of Gauss–Lobatto points in the radial direction, and we enforce the equations only in the interval $(0,R]$. For each Fourier mode, these equations are solved using a diagonalization technique in the two coordinates r and z . The imposed parity of the functions guarantees the regularity conditions at the origin needed to solve the Helmholtz equations [50].

In the finite volume code, a total number of about 610,000 control volumes were needed to obtain correctly converged results; we have checked the accuracy of the results with finer meshes, and found the error to be less than 1%. Typical time steps in these

Table 2
Typical thermophysical properties of the two binary fluids considered here and geometrical parameters.

Material	L (cm)	$2R$ (cm)	D (cm ² /s)	ν (cm ² /s)	Sc	$10^2 \beta_c \Delta C$	$10^3 Ra$ ($g = 1 \mu g$)	τ (s)
Photovoltaic Si	6	0.15	1×10^{-4}	3×10^{-3}	30	0.5	55.1	225
Al based alloy	6	0.15	0.2×10^{-4}	3×10^{-3}	150	-1	551	1125

cases are of the order of 10^{-5} . In the pseudospectral code we use $n_r = 42$, $n_z = 301$ and $n_\theta = 20$ points for radial, axial and azimuthal directions, test results have been checked with finer meshes and the maximum error in these cases is 0.07%. A time step of 10^{-3} suffices to obtain converged results in most of the computations, but has been decreased to 10^{-4} when needed.

As the initial conditions for the simulations, we consider the two halves of the cylinder at a uniform concentration of -0.5 and $+0.5$ respectively, with the fluid at rest. This initial condition is easily accomplished in the finite volume case but in the pseudo spectral code the abrupt central discontinuity has been approximated by a hyperbolic tangent profile.

$$C(0, r, \theta, z) = 0.5 \tanh[\delta(2\Gamma^{-1}z - 1)], \text{ where } z = [0, \Gamma]$$

with the parameter δ chosen as 300 for the resolution with $n_z = 301$.

The numerical results of the transport equations have then been post-processed trying to mimic each one of the two different experimental procedures reported in the literature for the obtention of the diffusion coefficients. In the first case (SC) the cell is considered to be formed by slices which, conveniently solidified, are analyzed at the end of the experiment to give a final average value of concentration (“post-mortem” analysis). In the second case (LC), the source of information comes from the instantaneous profiles of gray level all along the capillary generated by an X-ray analysis (“in situ” X-ray methodology). In both experimental procedures an estimated value of the diffusion coefficient $D^*(t)$ is obtained from the comparison of the numerical results with the analytical transient solution of the one dimensional diffusive problem with a constant diffusion coefficient in an infinite domain.

$$C(t, r, \theta, z) = -\frac{1}{2} \cdot \operatorname{erf}\left(-\frac{z}{2 \cdot \sqrt{D \cdot t}}\right),$$

where erf is the error function.

For the “post-mortem” indirect procedure, modeled by using the finite volume method, we define a standard cell with 20 slices. The mathematical post-processing is similar to the one presented in Refs. [2,3] so, the determination of $D^*(t)$ involves the calculation of the slope of the set of points $\{(z_i, 2 \cdot \sqrt{t} \cdot \operatorname{erf}^{-1}(-2 \cdot C_i(t, z_i)), \forall i = 1, 20\}$ by linear fitting. In this expression z_i is the position of the center of each segment of the cell, t the corresponding time, erf^{-1} the inverse of the Gauss error function, and

$$C_i(t, z_i) = \frac{1}{V_i} \cdot \int_{V_i} C(t, r, \theta, z) dV$$

the segment-averaged computed concentration. Calculations of $D^*(t)$ use only active segments in which the variation of the averaged concentration is greater than the 1% of the initial value. This choice is consistent with the 1% error threshold associated with the determination of the averaged concentration of each solidified slice of the shear cell by usual solid state techniques as, for example, Atomic Absorption Spectroscopy, Secondary Ion Mass Spectroscopy or Electron Probe Micro Analysis.

The long capillary methodology has been based on the pseudospectral method. The concentration values $C(t, r, \theta, z)$ obtained in each time step are cross-section averaged $\bar{C}(t, z)$ at each collocation point along the z -axis. After that we fit a concentration profile $(z, \bar{C}(t, z))$ to the error function profile by minimizing the least-squared error. $D^*(t)$ is finally calculated from the fit parameters. The evaluation of the error – in percentage – finally defines, in both cases, the following standard nondimensional indicator [14,15],

$$\%D^*(t) = 100 \cdot \frac{D^*(t) - D}{D} = 100 \cdot \left\{ \frac{D^*(t)}{D} - 1 \right\} \quad (2)$$

In order to satisfy the mathematical hypothesis of infinitely long domains, in the first case (“post-mortem” indirect procedure) calculations finished when the first and last segments become

simultaneously active. The time needed to attain these final conditions is called the end time, t_{end} and the final error associated to the process is $\%D^*(t_{\text{end}})$. In the second case (“in situ” direct procedure) the calculations finished when the averaged concentration in the z -axis first and last points, which correspond to the lids, also change more than 1% with respect to the initial value. These computational strategies avoid, in both cases, the necessity to consider the end time as a parameter to be simultaneously determined during the experiments, as it really occurs. Notice that the end times of both procedures will be slightly different.

Additional information concerning the purely diffusive case, equivalently, the stable configuration ($\alpha = 0$), shows that the quantitative value of the final indicator $\%D^*_{\text{diff}}(t_{\text{end}})$ in both procedures is low, of the order of 1.5, but not strictly zero. This value has been considered as a zero error inherent to the numerical methodology used and systematically subtracted from the $\%D^*(t)$ in each case. So, the corrected final indicator results as,

$$\%D(t_{\text{end}}) = \%D^*(t_{\text{end}}) - \%D^*_{\text{diff}}(t_{\text{end}}) \quad (3)$$

3. Results and discussion

3.1. Typical low and moderate solutal Rayleigh number environments

Fig. 2 displays the relative error in the determination of the diffusion coefficient $\%D(t_{\text{end}})$ as a function of the solutal Rayleigh number in the case in which the gravity and the initial density gradient are orthogonal. The results for the two values of the Schmidt numbers considered, 30 and 150, are practically identical and so only the calculations for $Sc = 150$ are plotted. In this figure, we have also included 2D results obtained in previous papers [2,3] for a rectangular cell of equivalent aspect ratio ($\Gamma = L/H$, being H the height of the cell) and the same values of the physical parameters. The 2D results were obtained using a finite volume scheme as the one used in the 3D calculations in order to model the SC technique. With respect to the 3D results, the presence of bounded walls in the third dimension introduces friction, which slows the convective motions produced by the interaction between the gradient of density and the orthogonal gravity. This fact promotes, in comparison with 2D results, higher values of the end time, t_{end} , and also $\%D(t_{\text{end}})$ values considerably lower [2,3]. If we compare the 3D results for the two techniques, 3D finite volume simulations in a cylinder modeling a 20 slices shear cell, SC(3D), and 3D pseudospectral method modeling the long capillary technique (LC), we obtain different end times (see Fig. 2(b)) and a difference in $\%D(t_{\text{end}})$ of the order of 0.25 at $Ra = 1500$.

In Table 3 we show how $\%D(t_{\text{end}})$ and t_{end} depend on the number of slices in the SC technique; increasing the number of slices, the numerical results of SC tend to the LC ones as one would expect. The results show that, in the orthogonal case, tridimensional considerations are mandatory in a more realistic discussion of the problem. In this way, the experimental threshold limit of the 1% is around $Ra = 625$ in the 2D case, but in the 3D case the value changes to be roughly twice, $Ra = 1250$. This means that, in terms of gravity values, the realistic threshold is located now around

Table 3

$\%D(t_{\text{end}})$ and t_{end} for different number of segments in the shear cell simulations. We also show the values obtained with the long capillary method ($n = \text{inf}$). All the results correspond to a solutal Rayleigh number $Ra = 1500$.

Segments	$\%D(t_{\text{end}})$	t_{end}
$n = 20$	1.2909	24.60
$n = 40$	1.4690	25.98
$n = 80$	1.5300	25.13
$n = \text{inf}$	1.5453	25.13

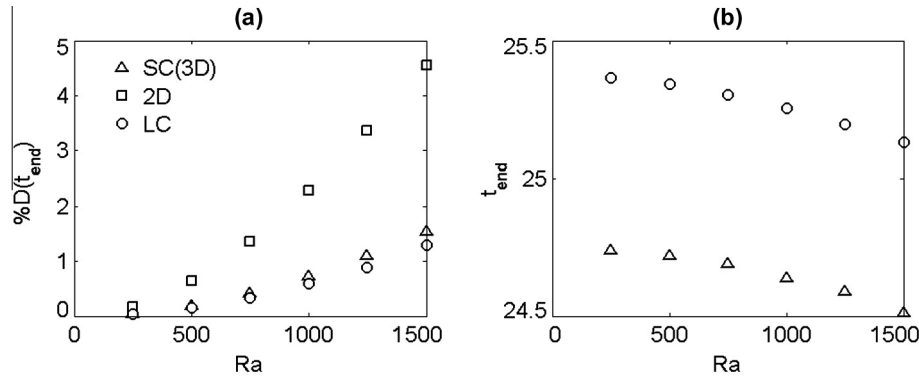


Fig. 2. Variation of the $%D(t_{end})$ values (a) and t_{end} (b) as a function of the solutal Rayleigh number for the shear cell method with $n=20$ segments (triangles), and pseudospectral simulations of the capillary cell (circles). The squares in (a) correspond to 2D simulations in a rectangular domain [2]. The gravity vector is acting orthogonally to the concentration gradient ($\alpha = \pi/2$).

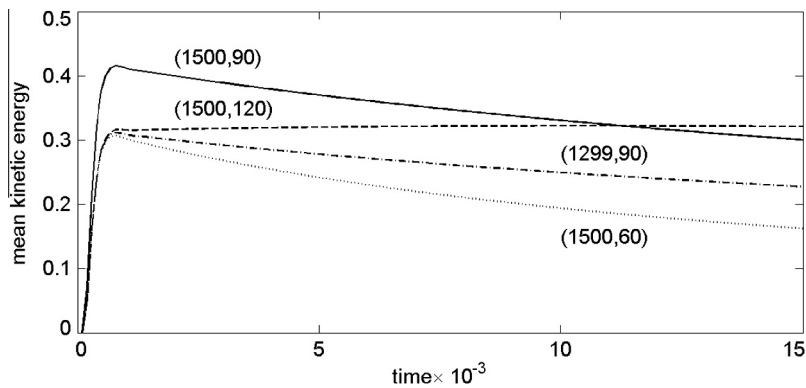


Fig. 3. Time evolution of the mean kinetic energy in a cylindrical cell for time instants close to $t = 0$. Three pairs of values of the Rayleigh numbers and orientations (Ra, α) with the same value of the x -component $Ra_x \approx 1299$ have been chosen: $(1500, 60^\circ)$, $(1500, 120^\circ)$, $(1299, 90^\circ)$. Results for $(1500, 90^\circ)$ have also been included for comparison.

1 mg. This change in the g level ensures a wider security range in which the experiment, located orthogonally, will present insensitivity to those types of constant microgravity levels.

Due to its relevance in experiments made in spacecrafts, we have studied the effect in the determination of $%D(t_{end})$ of the orientation of the gravity vector against the direction of the initial density gradient (see Fig. 1). For a gravity vector $\vec{g} = g_x \vec{i} + g_z \vec{k}$ or equivalently, $\vec{Ra} = Ra_x \vec{i} + Ra_z \vec{k}$, the initial driving is produced only by the interaction between the initial concentration profile $C(0,z)$ and the g_x component of the gravity vector. Once the initial profile of concentration is perturbed, an interaction of this perturbation with the g_z component arises, being its effect on the driving term dependent on the sign of g_z . If $g_z > 0$ ($\alpha < 90^\circ$) the initial driving is damped, in favor of the pure diffusive process, but if $g_z < 0$ ($\alpha > 90^\circ$) the initial driving is enhanced, in favor of the convective contamination. Therefore this nonlinear secondary effect depends on both components of the vector Rayleigh number, equivalently, on both components of the gravity vector. To clearly show this effect we present in Fig. 3 the time evolution of the mean kinetic energy in a cylindrical cell for time instants close to $t = 0$ (the time step has been reduced to capture the initial behavior). The calculations have been done modeling the LC methodology. Three pairs of values of the Rayleigh numbers and orientations (Ra, α) with the same value of the x -component, $Ra_x \approx 1299$, have been chosen: $(1500, 60^\circ)$, $(1500, 120^\circ)$, $(1299, 90^\circ)$. In all of them the initial driving is the same, but the immediate interaction with the z -component, Ra_z , is different. In the case of enhancing, the secondary nonlinear effect can even overcome a higher initial driving.

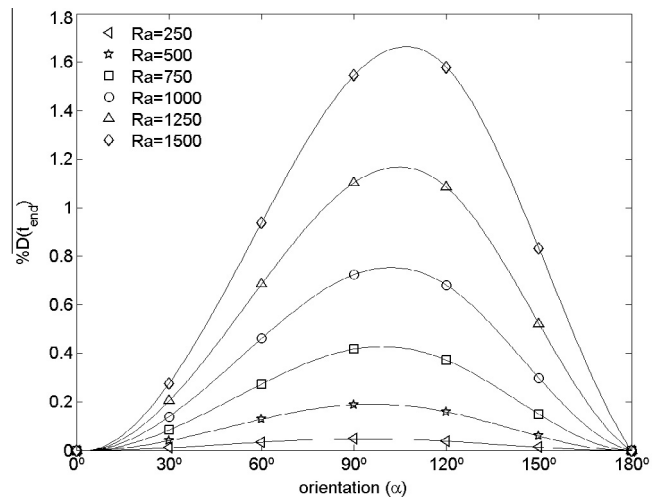


Fig. 4. Variation of the $%D(t_{end})$ values as a function of the relative orientation α between the gradient of concentration and the constant gravity vector, for different values of the Rayleigh number. The solid lines are spline interpolations of the data points.

This is what happens for example with the results for $(1500, 90^\circ)$, also shown in the same Fig. 3.

Fig. 4 shows the relative error in the determination of the diffusion coefficient $%D(t_{end})$ as a function of the orientation α for different values of the solutal Rayleigh number. Again, the results for the two values of the Schmidt number considered, 30 and 150, are

coincident. The results indicate that, according to the previous discussion, the relative error is asymmetric with respect to the orthogonal position. Clearly if the solutal Rayleigh value increases, the asymmetry degree becomes more pronounced. The position of the maximum value of the different $%D(t_{end})$ curves as the solutal Rayleigh number increases, shifts towards $\alpha = 180^\circ$. For the values of the solutal Rayleigh number of the figure, at $\alpha = 180^\circ$ the values of $%D(t_{end})$ are practically zero, because the Rayleigh number based on the length of the diffusion layer (L) is below the critical value for the onset of convection, i.e., no gravity-induced mixing exists. In the other side of the scale, $\alpha = 0^\circ$, the values of $%D(t_{end})$ go to zero according to the definition in Eq. (3).

The impact of the vibrations on the different experiments is another relevant problem in all kind of spacecrafts. To analyze it, we consider only the simplest ideal model in which gravity is a harmonic function of time given by $g(t) = A \cos(2\pi ft)$, acting orthogonally to the initial density gradient generated by the concentration step profile. Fig. 5(a), shows the values of $%D(t_{end})$ as a function of the external frequency f applied for two values of the Rayleigh number, 1500 and 3000, evaluated using the maximum gravity amplitude A (the results have been obtained modeling the LC method). Regardless of the value of the Schmidt number, calculations show that for the different vibrational Rayleigh numbers considered, the error does not decrease monotonically. For very low frequencies, the end time is lower than the period of the signal applied and $%D(t_{end})$ quickly decreases as the frequency increases, then the slope changes and $%D(t_{end})$ decreases more smoothly as the end time becomes greater than the period of the external oscillation. Based on this behavior it could be concluded that, in general, the convective contamination is mainly due to the ‘continuous part’ of the gravity signal; by removing it, the fluctuations will not affect the measure of the diffusion coefficient provided the frequency is high enough. It is interesting to note that the dimensional range of frequencies considered in our calculations is very low and that anti-vibratory mount strategies are more focused on damping vibrations of higher frequencies, in the vibratory range between 0.1 and 300 Hz (following the NASA’s definition concerning the International Space Station [54]). In Fig. 5(b) we show, for $Ra = 3000$, the results obtained modelling the LC and SC techniques, which corroborate the conclusions presented in the preceding cases.

We have also analyzed the effect of the rotation around the axis of the cylinder of the cell in the determination of the diffusion coefficient $%D(t_{end})$. The non-dimensional rotation rate Ω is considered constant during the process, the sign of Ω is not relevant because boundary conditions, initial condition and system of equations satisfy the following symmetry: if (u_r, u_θ, u_z) in (r, θ, z, t) is a solution of the problem for Ω , then $(u_r, -u_\theta, u_z)$ in (r, θ, z, t) is the solution of the problem for $-\Omega$. This symmetry implies that the measurement

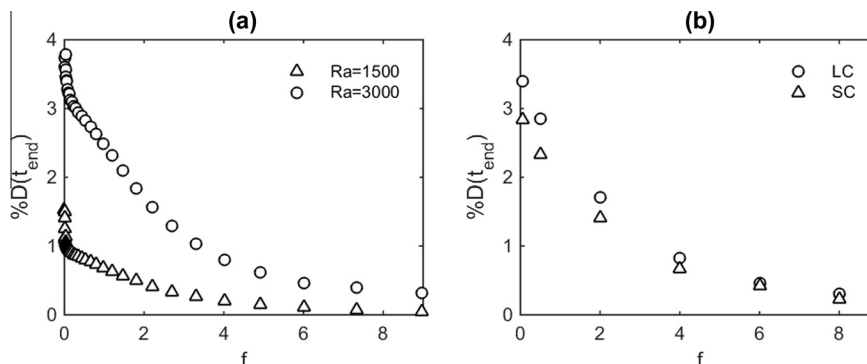


Fig. 5. (a) Variation of the $%D(t_{end})$ values as a function of the applied external harmonic frequencies for two different values of the Rayleigh number and perpendicular gravity field ($\alpha = 90^\circ$), $Ra = 1500$ (triangles) and $Ra = 3000$ (circles). (b) Values of $%D(t_{end})$ obtained modelling the two different experimental techniques: SC with $n = 20$ segments (triangles) and LC (circles), for $Ra = 3000$.

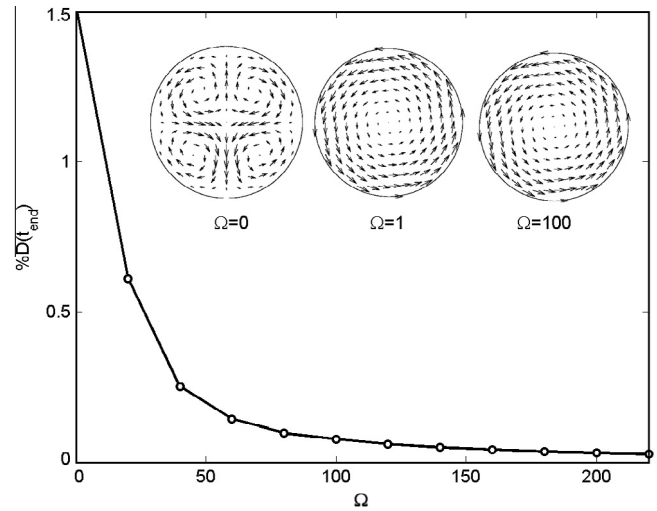


Fig. 6. $%D(t_{end})$ for different non dimensional axial angular velocities, for a fixed Rayleigh number ($Ra = 1500$) and perpendicular gravity field ($\alpha = 90^\circ$). The insets represent the transversal velocity field at the cylinder center plane for $\Omega = 0$, $\Omega = 1$ and $\Omega = 100$, the arrow length uses different scales in each figure. Note that the flow is already dominated by rotation for small values of Ω .

process is not affected by the sense of the rotation rate. We present here results obtained using the pseudospectral scheme modeling the LC methodology. We have solved the equations written in the inertial laboratory frame. The numerical scheme with respect the non rotating case is very easy to adapt because, as it is solved in cylindrical coordinates, we have only to modify the boundary condition of the azimuthal velocity on the walls. The results corresponding to a fixed value of the Rayleigh number $Ra = 1500$, maintaining the gravity field orthogonal to the initial concentration gradient, are depicted in Fig. 6. This figure clearly shows how the error $%D(t_{end})$ significantly decreases as the rotation rate increases. In the same figure we have represented the transversal velocity field near the $z = \Gamma/2$ plane for the case without rotation, $\Omega = 0$, and for $\Omega = 1$ and $\Omega = 100$. We can see that, already for $\Omega = 1$, the flow is dominated by the axial rotation of the cell. In order to better understand this mechanism, in Fig. 7(a) we have represented the maximum difference of the concentration in each plane or slice perpendicular to the cylinder axis, from the center ($z = \Gamma/2$) to the capillary end ($z = \Gamma$). The values reported correspond to the final state of the time evolution (t_{end}). As expected the maximum differences are observed near the center of the cell, where the initial concentration step is situated, and the maximum difference is reduced as the rotation rate increases due to the mixing induced by the azimuthal circulation of the fluid.

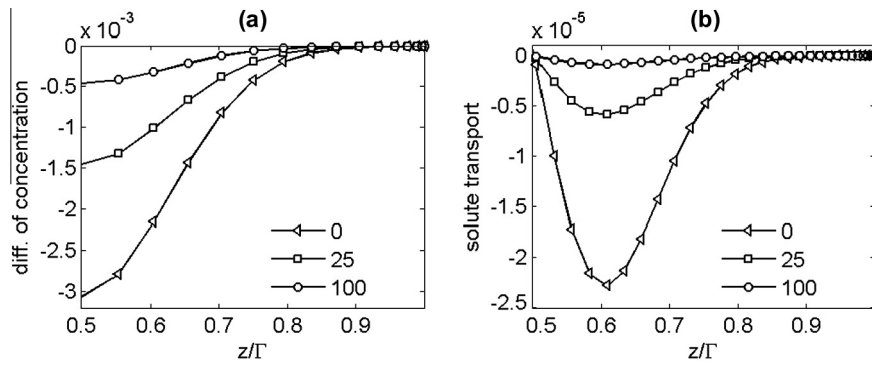


Fig. 7. (a) Maximum difference of concentration at $t = t_{\text{end}}$ in different planes $z = \text{const.}$ for $\Omega = 0$ (triangles), $\Omega = 25$ (squares) and $\Omega = 100$ (circles), the concentration variations decrease significantly as the rotation rate is increased. (b) Mean axial solute transport in the planes $z = \text{const.}$ for the same values of Ω .

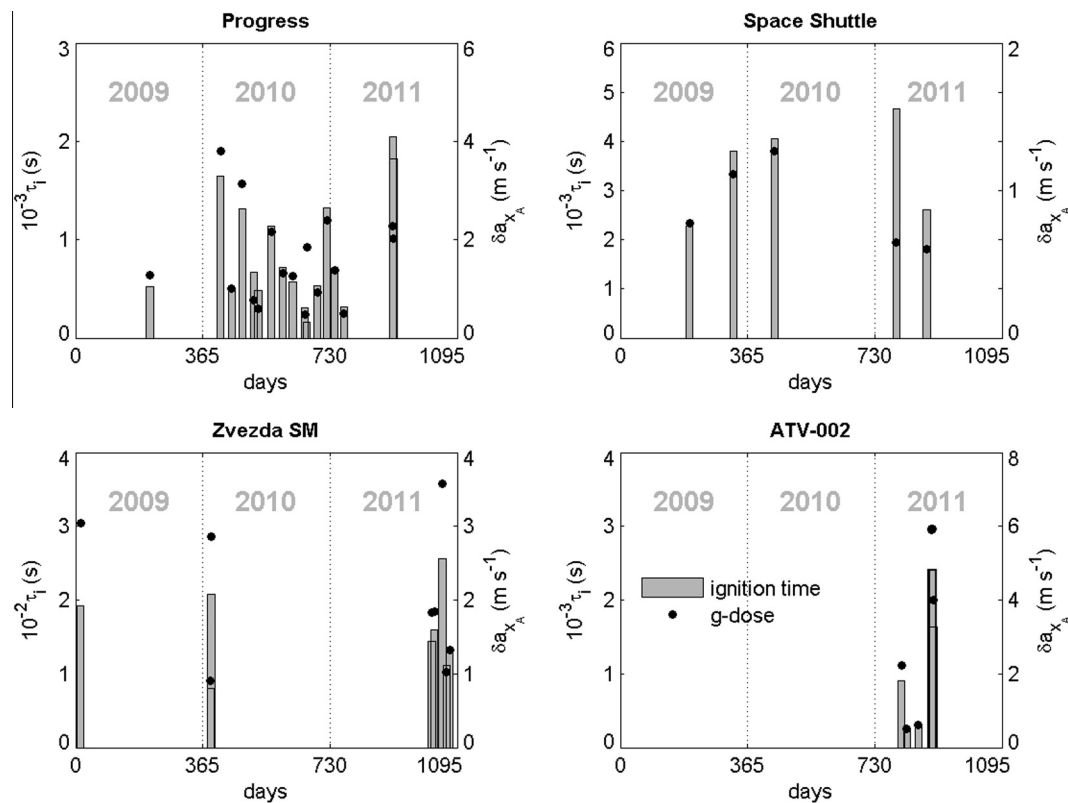


Fig. 8. Truster ignition time (left vertical axis, bars) and g-doses (right vertical axis, dots) corresponding to the X_A component of the different spacecrafts considered in the present study during the triennium 2009–2011.

In Fig. 7(b) we represent the mean axial convective solute transport at different $z = \text{const.}$ planes from the center to the end of the cell at $t = t_{\text{end}}$. The figure corroborates the expected result that solute transport diminishes as the rotation rate is increased. This is not a consequence of a reduction in the axial velocity, which in fact is not very much affected by the rotation, but a consequence of the homogenization of concentration that expels concentration from the regions with maximum axial velocity. The effect of the transversal homogenization is thus to reduce the axial solute transport, as shown in Fig. 7.

3.2. Implications on the International Space Station environment

The International Space Station, ISS, is the biggest and more complex orbiting object ever constructed in the space by the

humanity until now. With a mass of about 455 Metric Tons, it moves at an average speed of 27700 km/h (about 7.7 km/s) describing an elliptical orbit around the Earth. The eccentricity of this orbit is 0.0012, the orbital inclination is about 51.64° and the perigee and apogee are located at about 350 and 450 km to the Earth's surface respectively (Low Earth Orbit, LEO, type). The orbital period is about 92 min, equivalently, the Station makes about 15.6 revolutions around the Earth per day. However, all these orbital details are time dependent because the atmospheric drag generates an orbital decay of about 150 m per day. Periodical reboosts at intervals usually between ten and eighty days are necessary to increase the velocity for continuous Orbital Adjustments, OA. Reboosts/deboosts to increase/decrease the velocity for Debris Avoidance Manoeuvres, DAM, or to prepare more efficiently the rendezvous with resupply or crew transport spacecrafts.

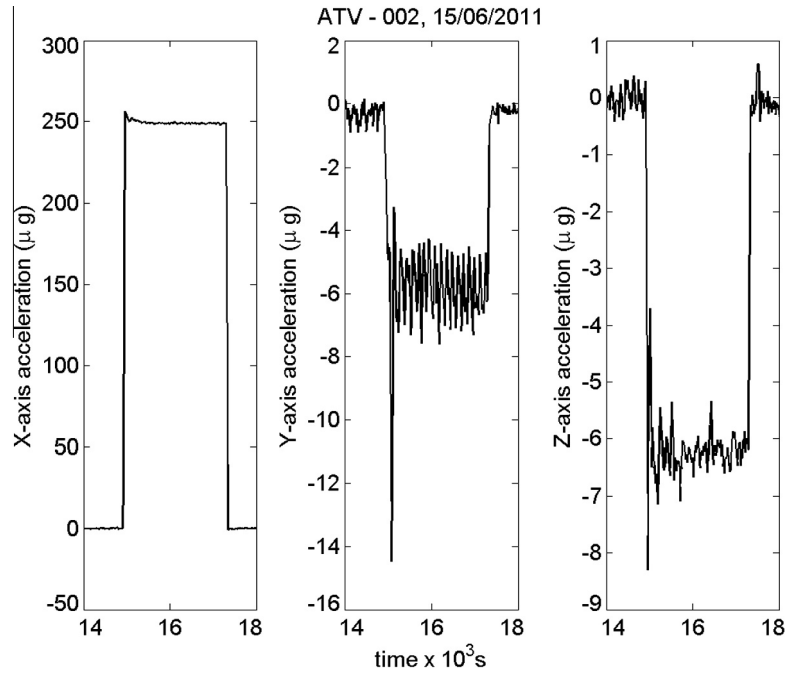


Fig. 9. SSA cartesian accelerometric components of a real reboosts finally selected (quasi-steady range).

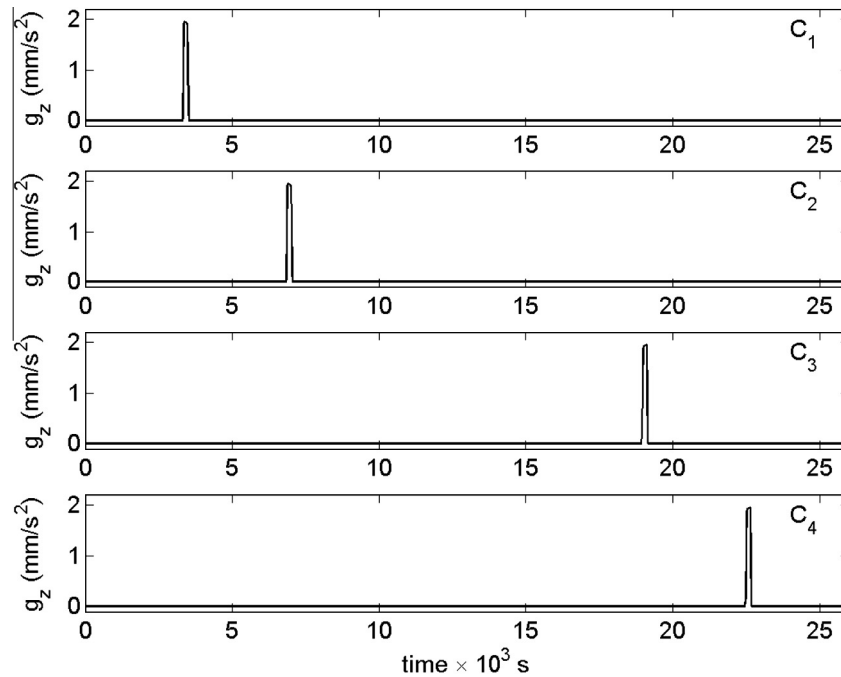


Fig. 10. The four different cases, C1, C2, C3 and C4 considered in the present work for the activation of the accelerometric signal.

Dockings and undockings as well as astro/cosmonaut spacewalks to build or repair parts of the Station configure a complete dynamic reality of that peculiar orbiting place [54–56].

In the present work, we concentrate on the last agitated period of the Station, 2009–2011. During this period the last Shuttle – Atlantis – undocked the Station in July the 19th of 2011 and during the above-mentioned triennium the Atlantis and the Endeavour docked the Station a total of three times each one, the Discovery docked four times and all together brought more than 150 Tones of modules and hardware to complete the Station [57–66]. Also,

the spacecrafts used for OA/DAM were different, i.e., Progress, ESA Automated Transfer Vehicles, different Shuttles and, sporadically, the Zvezda or the Zarya modules. Aiming to quantitatively investigate the accelerometric impact of these spacecrafts, we have firstly downloaded their corresponding quasi steady fingerprints from the MAMS ossbtmf sensor located in the Destiny module from PIMS NASA website [67]. The signals downloaded are originally trimmed filtered and bias compensated. The sampling rate is in all cases 0.0625 Hz and the cut-off frequency 0.01 Hz [68]. We concentrate here in the low frequency range because, from

Table 4
Results of the final $\%D(t_{\text{end}})$ indicator for the different spacecrafts considered. C1, C2, C3 and C4 refer to the signals displayed in Fig. 10.

Vehicle	Date	τ_i (s)	$\delta a(x_A)$ (m/s)	$\delta a(y_A)$ (m/s)	$\delta a(z_A)$ (m/s)	$\%D(t_{\text{end}})$			
						C1	C2	C3	C4
Progress	23/04/2010	1312	0.08	0.08	3.13	$<1 \times 10^{-3}$	$<1 \times 10^{-3}$	$<2 \times 10^{-3}$	$<2 \times 10^{-3}$
Shuttle Endeavour	18/02/2010	4064	0.058	0.032	1.27	$<1 \times 10^{-3}$	$<1 \times 10^{-3}$	$<1 \times 10^{-3}$	$<2 \times 10^{-3}$
ATV-002	17/06/2011	1632	0.09	0.09	4.0	$<2 \times 10^{-3}$	$<2 \times 10^{-3}$	$<5 \times 10^{-3}$	$<7 \times 10^{-3}$
Zvezda	24/01/2011	208	0.053	0.1	2.86	$<1 \times 10^{-3}$	$<2 \times 10^{-3}$	$<3 \times 10^{-3}$	$<3 \times 10^{-3}$
Zarya	29/09/2011	224	0.049	0.053	2.84	$<6 \times 10^{-3}$	$<6 \times 10^{-3}$	$<8 \times 10^{-3}$	$<9 \times 10^{-3}$

the point of view of fluid mechanics in general, this is the most pernicious one [69,70]. In addition, recent literature indicates that the vibratory range – equivalently SAMS signals – do not impact in a relevant way the diffusion coefficient measurements at all [71–74]. Finally, it is worth mentioning that the rest of disturbances, dockings, undockings and Extra Vehicular Activities show accelerometric levels considerably lower than the OA/DAM ones, so they have been initially discarded.

The reference used here to quantify the problem is the Space Station Analysis coordinate system, SSA. This is an orthonormal one with the Z_A axis pointing toward the center of the Earth (Nadir direction). The X_A axis coincides with the line of manned modules and Y_A axis coincides with the line of the Integrated Truss Structure, ITS. The X_A axis is considered positive, $+X_A$, going from the Zvezda to the Harmony modules. In the same way, the Y_A axis is considered positive going from the P6 to the S6 Truss Segments [54–56,75]. The origin of coordinates is located in the center of mass of the Station, a point actually located in the S0 Truss segments. To characterize the different signals we use their g -doses in m/s related to the above-mentioned SSA reference. In this way, the g -dose corresponding to the X_A component is defined as

$$\delta a(X_A)(t) = \int_t^{t+\tau_i} |a_x(t)| \cdot dt$$

and, by its definition, it is equivalent to the variation of velocity in this period of time, a typical measure of the change of velocity used for fly controllers in Orbiter Adjustments. Fig. 8 shows that during the three-year period under study the maximum positive values of the X_A accelerometric doses for Progress and ATV spacecrafts are of the same order than the Zarya or Zvezda ones; however, the thruster ignition time, τ_i , is higher in the two first cases as a consequence of the resupply character of both spacecrafts. In the case of the five Shuttle reboosts the values are considerably lower than rest of spacecrafts. This is because only the Reaction Control System, RCS, was used for OA/DAM. This system comprises three groups of primary and Vernier small jets located in the forward fuselage and in two independent pods located on each side of the vertical tail of the orbiter's aft fuselage. The pods also house the aft Orbital Maneuvering System, OMS, and were usually referred as the OMS/RCS pods. As for the g -doses corresponding to the Y_A and Z_A -axes, their values are, in all cases, very low against the corresponding X_A ones, so, their impact will be very small.

Based on the information summarized in Fig. 8 and in order to analyze the impact of the OA/DAM manoeuvres on the accuracy of the measurements of the diffusion coefficients, we have selected five scenarios, one for each spacecraft, with high values of the X_A g -dose. Fig. 9 explicitly shows, as an example, one of the five quasi-steady signals selected. The three accelerometric components of the signals have been introduced in the 3D numerical computation, taking into account that the signal of the X_A sensor was applied to the Z axis of the shear cell, which is the worst case. In addition, to be as exhaustive as possible, each scenario activates the perturbation at different times of the diffusion process. Fig. 10 clarifies the four situations concerning only the acceleration

introduced in the Z axis. The other two components of acceleration were activated for calculations at the same time as X_A was. The final results are synthesized in Table 4, but only in the case of Al-based alloys; the values of $\%D(t_{\text{end}})$ of the four signals are always below the resolution limits of the experiments, a slight increase of the percentage of error seems to exist as a function of the time instant at which the perturbation is applied. This is a consequence of the fact that the flow has increasingly less time to relax the impact of the different reboosting episodes. Finally, it is worth mentioning that because the rest of disturbances have small accelerometric levels, from the present analysis we can conclude that these kinds of disturbances have definitively no impact on the accuracy of the diffusion coefficient measurements, neither in doped PV-Si melts nor in Al-based alloys.

4. Conclusions

We have studied the effect of convective fluid motions on the measurement of mass diffusion coefficients of liquid Al-based alloys and doped photovoltaic silicon, using capillary cylindrical cells. Our analysis have considered low solutal Rayleigh numbers corresponding to experiments made in orbiting laboratories. On one hand, we have used a 3D finite volume code to gain experience in the simulation of the flow behavior of a twenty segment shear cell; on the other, a pseudospectral 3D code enabled us to calculate instantaneous and continuous concentration profiles all along the capillary. These profiles have been used, as it would have been done in real capillary cell experiments, to estimate an apparent diffusion coefficient concerning melt dopants or two-component mixtures. We report in both, shear cells and capillaries, the error introduced by the convective bulk flow generated by a number of different gravity conditions. Calculations indicate that the relevant disturbing thresholds are always located in the level of mg . In addition we have also analyzed in detail the effect of harmonic disturbances of very low frequencies. The results indicate that the $\%D(t_{\text{end}})$, always decreases monotonically with increasing frequency. Also, the effect of rotating the cell along the cylindrical axis has been proved to be an extremely effective way of suppressing the mass transport due to convection. The numerical simulations show exactly that $\%D(t_{\text{end}})$ quickly diminishes as the rotation rate increases. Finally, we have discussed in detail how real microgravity conditions onboard the ISS during the last agitated period of building of the Station can affect the measurement of diffusion coefficients. The conclusion in both cases, shear cells and capillaries, is very favorable in the sense that even under the influence of these strong ISS transient disturbances, no convective impact has been detected in all the calculations. Equivalently, the $\%D(t_{\text{end}})$ values obtained are always far below the experimental limit of detection, the 1% threshold.

Conflict of interest

None declared.

Acknowledgements

The authors acknowledge the financial support of the DGICYT grant FIS2013-40880-P. Also, one of the authors, O. Sánchez, was supported by a FI grant from the DGR of the Generalitat de Catalunya. The content of the present work was also part of our participation in the HSF-US/2010-042 and HSF-US/2010-041 ESA projects.

References

- [1] G. Mathiak, A. Griesche, K.H. Kraatz, G. Froberg, Diffusion in liquid metals, *J. Non-Cryst. Solids* 205–207 (1996) 412–416.
- [2] X. Ruiz, J. Pallarés, F.X. Grau, On the accuracy of the interdiffusion measurements at low and moderate Rayleigh numbers. A computational approach, *Int. J. Heat Mass Transfer* 53 (2010) 3708–3720.
- [3] X. Ruiz, J. Pallarés, On the accuracy of the diffusion coefficient measurements using different initial shear cell configurations at low and moderate Rayleigh numbers, *Int. J. Heat Mass Transf.* 55 (2012) 6966–6978.
- [4] A. Dario, H.O. Sicim, E. Balicki, Germanium-silicon single crystal growth by the axial heat processing (AHP) technique, *J. Cryst. Growth* 318 (2011) 1057–1061.
- [5] A. Griesche, F. Garcia, M.-P. Moreno, G. Froberg, Chemical diffusion experiments in AlNiCe-melts, *Mater. Sci. Forum* 508 (2006) 567–572.
- [6] A. Griesche, B. Zhang, J. Horbach, A. Meyer, Atomic diffusion and its relation to thermodynamic forces in Al-Ni melts, *Defects and Diffusion Forum* 289–292 (2009) 705–710.
- [7] B. Zhang, A. Griesche, A. Meyer, Diffusion in Al-Cu melts studied by time-resolved X-ray radiography, *Phys. Rev. Lett.* 104 (2010). 035902 – 035902-4.
- [8] A.G. Ostrogorsky, Numerical simulation of single crystal growth by submerged heater method, *J. Cryst. Growth* 104 (1990) 233–238.
- [9] A.G. Ostrogorsky, G. Müller, Normal and zone solidification using the submerged heater method, *J. Cryst. Growth* 137 (1994) 64–71.
- [10] S.V. Bykova, V.D. Golyshv, M.A. Gonik, V.B. Tsevetosky, E. Balicki, A. Deal, R. Abbaschian, M.P. Marchenko, I.V. Frjazinov, V.N. Vlasov, J.A. Serebrjakov, The experimental-numerical investigation of instability of faceted Ge doped by Sb growth on the base of AHP method, *J. Cryst. Growth* 275 (2005) e229–e236.
- [11] M.A. Gonik, A.V. Lomokhova, M.M. Gonik, A.T. Kuliev, A.D. Smirnov, Development of a model for on-line control of crystal growth by the AHP method, *J. Cryst. Growth* 303 (2007) 180–186.
- [12] M.P. Marchenko, V.D. Golyshv, S.V. Bykova, Investigation of $Cd_{1-x}Zn_x$ composition inhomogeneity at crystal growth by AHP-method, *J. Cryst. Growth* 303 (2007) 193–198.
- [13] J. P. Praizey, J. P. Garandet, G. Froberg, A. Griesche K-H. Kraatz, Diffusion experiments in liquid metals. Preliminary results (AGAT-Module on FOTON12), in: O. Minster, B. Schürmann (Eds.), Proceedings of the First International Symposium on Microgravity Research and Applications in Physical Sciences and Biotechnology, Sorrento, Italy, 2001, pp. 481–490.
- [14] T. Itami, A. Mizuno, H. Aoki, Y. Arai, K. Goto, S. Amano, N. Tateiwa, M. Kaneko, T. Fukazawa, R. Nakamura, H. Nishioji, A. Ogiso, T. Nakamura, Y. Nakamura, N. Koshikawa, T. Masaki, M. Natsuzaka, S. Matsumoto, S. Munejiri, M. Uchida, S. Yoda, The study of diffusion in complex metallic liquids with high meeting points. The study of self-diffusion and mutual-diffusion of liquid Cu-Ag alloys, *J. Jpn. Soc. Microgravity Appl.* 17 (2000) 64–69.
- [15] R.W. Smith, The influence of g-jitter on liquid diffusion. The QUELD/MIM/MIR programme, *Microgravity Sci. Technol.* XI (2) (1998) 78–84.
- [16] R. W. Smith, X. Zhu, M. C. Tunncliffe, T.J.N. Smith, L. Misener, J. Adamson, The measurement of precise solute diffusion coefficients in dilute liquid metals and metalloids in a low earth orbiting laboratory. The influence of g-jitter, in: O. Minster, B. Schürmann (Eds.), Proceedings of the First International Symposium on Microgravity Research and Applications in Physical Sciences and Biotechnology. Sorrento, Italy, 2001, pp. 887–893.
- [17] R.W. Smith, X. Zhu, M.C. Tunncliffe, T.J.N. Smith, L. Misener, J. Adamson, The influence of gravity on the precise measurement of solute diffusion coefficient in dilute liquid metals and metalloids, *Ann. N.Y. Acad. Sci.* 974 (2002) 57–67.
- [18] B.V. Tryggvason, R.F. Redden, R.A. Herring, W.M.B. Duval, R.W. Smith, K.S. Rezkallah, S. Varma, The vibration environment on the International Space Station: its significance to fluid-based experiments, *Acta Astronaut.* 46 (2001) 59–70.
- [19] R. Savino, D. Paterna, Compatibility of the microgravity environment of the International Space Station with fluid and material science experimentation, *Acta Astronaut.* 51 (2002) 229–241.
- [20] R. Monti, R. Savino, D. Paterna, The fluid-dynamic disturbances induced on the ISS, based on the first acceleration measurements on board the space station, *Acta Astronaut.* 57 (2005) 22–30.
- [21] R. Monti, R. Savino, D. Paterna, On a more rational specification for the microgravity environment of the International Space Station, *Acta Astronaut.* 58 (2006) 197–208.
- [22] F. Barvinschi, C. Stelian, Y. Delannoy, N. Mangelinck, T. Duffar, Modelling the multi-crystalline silicon ingot solidification process in a vertical square furnace, *J. Optoelectron. Adv. Mater.* 5 (2003) 293–300.
- [23] Y. Delannoy, F. Barvinschi, T. Duffar, 3D dynamic mesh numerical model for multi-crystalline silicon furnaces, *J. Cryst. Growth* 303 (2007) 170–174.
- [24] D. Vizman, J. Friedrich, G. Mueller, 3D time-dependent numerical study of the influence of the melt flow on the interface shape in a silicon ingot casting process, *J. Cryst. Growth* 303 (2007) 231–235.
- [25] B. Wu, N. Stoddard, R. Ma, R. Clark, Bulk multicrystalline silicon growth for photovoltaic (PV) application, *J. Cryst. Growth* 310 (2008) 2178–2184.
- [26] A.T. Kuliev, N.V. Durnev, V.V. Kalaev, Analysis of 3D unsteady melt flow and crystallization front geometry during a casting process for silicon solar cells, *J. Cryst. Growth* 303 (2007) 238–240.
- [27] L. Liu, S. Nakano, K. Kakimoto, Dynamic simulation of temperature and iron distributions in a casting process for crystalline silicon solar cells with a global model, *J. Cryst. Growth* 292 (2006) 515–518.
- [28] H. Matsuo, R.B. Ganesh, S. Nakano, L. Liu, Y. Kangawa, K. Arafune, Y. Ohshita, M. Yamaguchi, K. Kakimoto, Thermodynamical analysis of oxygen incorporation from quartz crucible during solidification of multicrystalline silicon for solar cell, *J. Cryst. Growth* 310 (2008) 4666–4671.
- [29] B. Gao, X.J. Chen, S. Nakano, K. Kakimoto, Crystal growth of high-purity multicrystalline silicon using a unidirectional solidification furnace for solar cells, *J. Cryst. Growth* 312 (2010) 1572–1576.
- [30] N. Dropka, W. Miller, R. Menzel, U. Rehse, Numerical study on transport phenomena in a directional solidification process in presence of travelling magnetic field, *J. Cryst. Growth* 312 (2010) 1407–1410.
- [31] T. Liu, Z. Dong, Y. Zhao, J. Wang, T. Chen, H. Xie, J. Li, H. Ni, D. Huo, Purification of metallurgical silicon through directional solidification in a large cold crucible, *J. Cryst. Growth* 355 (2012) 145–150.
- [32] Ch.-A. Gandin, J.-L. Desbiolles, M. Rappaz, Ph. Thevoz, A three-dimensional cellular automaton-finite element model for the prediction of solidification grain structures, *Metall. Mater. Trans. A* 30 (1999) 3153–3165.
- [33] J. Friedrich, R. Backofen, G. Müller, Numerical simulation of formation of grain structure and global heat transport during solidification of technical alloys in MSL inserts, *Adv. Space Res.* 29 (2002) 549–662.
- [34] P. Sickinger, H.-G. Bernhardt, K-H. Kraatz, A. Griesche, G. Froberg, AGAT – A FOTON furnace facility, in: O. Minster, B. Schürmann (Eds.), Proceedings of the First International Symposium on Microgravity Research and Applications in Physical Sciences and Biotechnology. Sorrento, Italy, 2001, pp. 895–896.
- [35] W.A. Arnold, D. Matthiesen, Numerical simulation of the effect of shearing on the concentration profile in a shear cell, *J. Electrochem. Soc.* 142 (1995) 433–438.
- [36] D.H. Matthiesen, K. Davidson, W.A. Arnold, Physical Modeling of the Effect of Shearing on the Concentration Profile in a Shear Cell, *J. Electrochem. Soc.* 146 (1999) 3087–3091.
- [37] X. Ruiz, J. Pallares, F.X. Grau, FLUENT under microg conditions, VII Forum FLUENT Madrid, Spain, 2006.
- [38] B. Wu, S. Scott, N. Stoddard, R. Clark, A. Sholapurwalla, Simulation of silicon casting process for photovoltaic (PV) application, The Mineral, Metals & Materials Society, 2009.
- [39] L. Liu, S. Nakano, K. Kakimoto, Dynamic simulation of temperature and iron distributions in casting process for crystalline silicon solar cells with a global model, *J. Cryst. Growth* 292 (2006) 515–518.
- [40] D. Vizmann, 3D time-dependent numerical study of the influence of the melt flow on the interface shape in a silicon ingot casting process, *J. Cryst. Growth* 303 (2007) 231–235.
- [41] J.P. Garandet, New determinations of Diffusion Coefficients for various dopants in liquid silicon, *Int. J. Thermophys.* 28 (2007) 1285–1303.
- [42] K.-H. Lee, Axial distribution of Gallium and Silicon crystals for photovoltaic applications, *Jpn. J. Appl. Phys.* 46 (2007) 2831–2854.
- [43] J. Brillo, I. Egly, J. Westphal, Density and thermal expansion of liquid binary Al-Ag and Al-Cu alloys, *Int. J. Mater. Res.* 99 (2008) 162–167.
- [44] A. Griesche, B. Zhang, J. Horbach, A. Meyer, Atomic diffusion and its relation to thermodynamic forces in Al-Ni melts, *Defect Diffus. Forum* 289–292 (2009) 705–710.
- [45] J.P. Garandet, G. Mathiak, V. Botton, P. Lehmann, A. Griesche, Reference microgravity measurements of liquid phase solute diffusivities in Tin- and Aluminum-based alloys, *Int. J. Thermophys.* 25 (2004) 249–272.
- [46] A. Griesche, F. García-Moreno, M.-P. Macht, G. Froberg, Chemical diffusion experiments in AlNiCe-melts, *Mater. Sci. Forum* 508 (2006) 567–572.
- [47] J. Pallarés, I. Cuesta, F.X. Grau, Laminar and turbulent Rayleigh-Bénard convection in a perfectly conducting cubical cavity, *Int. J. Heat Fluid Flow* 23 (2002) 346–358.
- [48] Numerical. Recipes, The Art of Scientific Computing, Cambridge University Press, 2007.
- [49] I. Mercader, O. Batiste, A. Alonso, An efficient spectral code for incompressible flows in cylindrical geometries, *Comput. Fluids* 39 (2010) 215–224.
- [50] S. Hugues, A. Randriamampianina, An improved projection scheme applied to pseudospectral methods for the incompressible Navier–Stokes equations, *Int. J. Numer. Methods Fluids* 28 (1998) 501–521.
- [51] G.E. Karniadakis, M. Israeli, S.A. Orszag, High Order Splitting Methods for the Incompressible Navier–Stokes Equations, *J. Comput. Phys.* 97 (1991) 414–443.
- [52] B. Fornberg, A Practical Guide to Pseudospectral Methods, Cambridge University Press, 1998.
- [53] L.N. Trefethen, Spectral Methods in Matlab, SIAM, 2000.
- [54] K. Jules, Working in a Reduced-gravity Environment: A Primer, NASA 7th Annual Microgravity Environment Interpretation Tutorial, NASA Glenn Research Center, Ohio Aerospace Institute, Cleveland, Ohio, 2004.
- [55] E. Ceglia, European Users Guide to Low Gravity Platforms, UIC-ESA-UM-0001. Issue 2 Revision 0, 2005.

- [56] Reference guide to the INTERNATIONAL SPACE STATION, Assembly Complete Edition, November 2010. NASA Document NP-2010-00-682 HQ.
- [57] <http://www.nasa.gov/pdf/304681main_STS-119_Press_Kit.pdf> (STS 119, Press Kit, February 2009. NASA).
- [58] <http://www.nasa.gov/pdf/358018main_sts127_press_kit.pdf> (STS-127, Press Kit, June 2009, NASA).
- [59] <http://www.nasa.gov/pdf/379392main_STS-128_Press_Kit.pdf> (STS-128, Press Kit, August 2009. NASA).
- [60] <http://www.nasa.gov/pdf/397216main_sts129_presskit.pdf> (STS-129, Press Kit, October 2009. NASA).
- [61] <http://www.nasa.gov/pdf/423514main_sts130_press_kit_2.pdf> (STS-130, Press Kit, January 2010. NASA).
- [62] <http://www.nasa.gov/pdf/435885main_sts131_press_kit.pdf> (STS-131, Press Kit, April 2010. NASA).
- [63] <http://www.nasa.gov/pdf/451029main_sts132_press_kit2.pdf> (STS-132, Press Kit, May 2010. NASA).
- [64] <http://www.nasa.gov/sites/default/files/files/491387main_STS-133.pdf> (STS-133, Press Kit, February 2011. NASA).
- [65] <http://www.nasa.gov/mission_pages/shuttle/shuttlemissions/sts134/> (STS-134, Press Kit, April 2011. NASA).
- [66] <http://www.nasa.gov/pdf/566071main_135_press_kit2.pdf> (STS-135. Press Kit, July 2011. NASA).
- [67] <<http://pims.grc.nasa.gov/html/ISSAccelerationArchive.html>>.
- [68] E. Kelly, International Space Station (ISS) Measured Quasi-Steady Environment, NASA 7th Annual Microgravity Environment Interpretation Tutorial, NASA Glenn Research Center, Cleveland, Ohio, 2004.
- [69] E. Nelson, Predicting Residual Acceleration Effects on Space Experiments, NASA 7th Annual Microgravity Environment Interpretation Tutorial, NASA Glenn Research Center, Cleveland, Ohio, 2004.
- [70] A. Ahadi, M.Z. Saghir, Quasi steady state effect of micro vibration from two space vehicles on mixture during thermodiffusion experiment, *Fluid-Dyn. Mater. Process.* 8 (2012) 397–422.
- [71] Y. Yan, S. Pan, K. Jules, M.Z. Saghir, Vibrational effect on thermal diffusion under different microgravity environments, *Microgravity Sci. Technol.* XIX (2) (2007) 12–24.
- [72] A. Ahadi, M.Z. Saghir, Transient effect of micro vibration from two space vehicles on mixture during thermodiffusion experiment, *Microgravity Sci. Technol.* 25 (2013) 127–139.
- [73] N. Sáez, X. Ruiz, J. Pallarés, V. Shevtsova, On the accuracy of the interdiffusion coefficient measurements of high temperature binary mixtures under real ISS conditions, *Comptes Rendus Mécanique* 341 (2013) 405–416.
- [74] A. Khoshnevis, A. Ahadi, M.Z. Saghir, Influence of Static and Oscillatory gravity fields on thermodiffusion of a binary mixture, *Int. J. Therm. Sci.* 75 (2014) 221–232.
- [75] K. Jules, K. Hrovat, E. Kelly, T. Reckart, International Space Station Increment -6/8. Microgravity Environment. Summary Report, 2006 (NASA TM-2006-213896).